https://doi.org/10.5194/hess-2023-190
Preprint. Discussion started: 29 August 2023

Hydrology and Earth System Sciences
Discussions
Open Access
EGU

Combining time-lapse electrical resistivity and self-potential methods to assess soil moisture dynamics in a forested catchment under the rainfall event

Wenhang Jiang[1,3], Aimin Liao[1,2], Jiufu Liu[1], Guodong Liu[3]

[1]State Key Laboratory of Hydrology-Water Resource and Hydraulic Engineering, Nanjing Hydraulic Research Institute, Nanjing, PR China;
[2]Chuzhou Scientific Hydrology Laboratory, Nanjing Hydraulic Research Institute, Chuzhou, PR China;
[3]State Key Laboratory of Hydraulics and Mountain River Engineering, Sichuan University, Chengdu, PR China

Correspondence to: Aimin Liao (seamsun1226@163.com)

Abstract. Infiltration process and soil moisture dynamics in response to rainfall are crucial for subsurface flow generation, landslide hazard control, and hydro-ecosystem management. Geophysical tools such as the electrical resistivity tomography (ERT) and self-potential (SP) method have proven useful in providing greater temporal and spatial subsurface information and making connections to water content or water flux. In this study, the combination of ERT and SP was used to enhance our understanding of water infiltration processes caused by natural rainfall, subsurface structures, and plant root distribution. We installed 100 ERT electrodes with an electrode spacing of 0.5 m on a tree-covered hillslope to conduct ERT surveys every two weeks from June to October 2022, and increase the frequency of measurements during rainfall events. Non-polarized electrodes were used to measure SP along the hillslope and at various depths. Time-domain reflectometry (TDR) sensors were used to obtain the soil water content as an accurate reference to establish the petrophysical relationship between soil moisture and resistivity. Based on the robustness assessment of these relationships, the results suggest that the Dipole-Dipole configuration may help to obtain a more reasonable interpretation of resistivity at the forest site than the Wenner configuration. The joint interpretation of the SP and ERT results showed that water flow in the study area is dominated by vertical direction, and two preferential flow paths due to the fractured and permeable soil layer interface provide important vertical hydrological connections between deep and shallow soil layers. In addition, the subsurface infiltration processes were strongly influenced by the trees with different root characteristics. Trees with shallow roots tend to retain more water content at the surface. Deep-rooted trees absorb and store water in deeper layers, resulting in significant abrupt

https://doi.org/10.5194/hess-2023-190
Preprint. Discussion started: 29 August 2023

Hydrology and Earth System Sciences
Discussions
Open Access
EGU

changes in the water content of the deeper soil layers. The results of this study provide a basis for investigating the hydrological connectivity and climate sensitivity of soil water distribution by linking rainfall with subsurface information provided by the ERT and SP.

https://doi.org/10.5194/hess-2023-190
Preprint. Discussion started: 29 August 2023

Hydrology and Earth System Sciences
Discussions

1 Introduction

Precipitation is the most direct and significant source of soil water recharge. Characterizing the effects of precipitation on the infiltration process and soil moisture is critical for the prediction of hydrological pathways (Tetzlaff et al., 2014; Zeng et al., 2016; Hermans et al., 2023), landslide hazard control (Hojat et al., 2019; Nielson et al., 2021; Tsai et al., 2021) and hydro-ecosystem management (Carey et al., 2019). In addition, subsurface structure, vegetation canopies, and highly distributed roots can be the significant contributors to the flow, leading to heterogeneity in soil moisture distribution and associated dynamics (Holbrook et al., 2014; Dick et al., 2018; Vanella et al., 2018). Due to the lack of appropriate tools and the heterogeneity of soil properties in the subsurface, the water dynamics of fluxes and processes and their influences remain poorly understood. Several studies have addressed the dynamics of rainfall infiltration (Cassiani et al., 2009, Travelletti et al., 2012, Carey et al., 2019), moisture variability due to hydraulic redistribution (Robinson et al., 2012; Ain-Lhout et al., 2016; Dick et al., 2018; Guo et al., 2020), soil-root interactions (Garré et al., 2011; Amato et al., 2008; Vanella et al., 2018), and the influence of subsurface structures (Holbrook et al., 2014; Hermans et al., 2023). However, few studies have simultaneously concerned the above multiple influences during the rainfall infiltration process, especially the effects of root characteristics between different tree species on water distribution. This is of great interest in bridging the gap between common modeling approaches and field realities.

Soil moisture dynamics in the subsurface are particularly difficult to characterize. These processes are typically measured using a gravimetric analysis, isotopic tracing, or in situ sensors such as time-domain reflectometry (TDR). These point data or low sampling density prevented a full description of the dynamics of hydrological processes and structures with a high spatial resolution (Zhou et al., 2001; Tetzlaff et al., 2014; Parsekian et al., 2015). Geophysical techniques such as electrical resistivity tomography (ERT) (Srayeddin and Doussan, 2009; Robinson et al., 2012; Beff et al., 2013; Fan et al., 2020; Nielson et al., 2021) and self-potential (SP) (Doussan et al., 2002; Suski et al., 2006; Revil et al., 2012; Voytek et al., 2016, 2019) have been proven to be useful in providing minimally invasive ways to visualize the hydrogeological processes. Cassiani et al. (2009) and Carey et al. (2019) observed the evolution of the wetting peak evolution under transient unsaturated conditions with ERT, when rainfall occurred over a fixed rainfall simulator location (not the entire slope). However, the natural rainfall often

https://doi.org/10.5194/hess-2023-190
Preprint. Discussion started: 29 August 2023

Hydrology and Earth System Sciences
Discussions
Open Access
EGU

occurs over the entire slope, making it difficult to use ERT alone to determine whether the wetting evolution is dominated by lateral subsurface flow or vertical infiltration flow. The SP method has been found to be a complementary methods in characterizing subsurface water flow. Richards et al. (2010) used the ERT and SP and identified nine preferential flow paths in faults. Voytek et al. (2016) identified the hydrologic flowpaths on arctic hillslopes using ERT and SP and provided greater insight into how flow paths and the frost boundary interrelate. However, the combination of the two approaches has rarely been highlighted for investigating the spatial-temporal variation of the subsurface flow in response to rainfall events in the forested site.

In the study of soil moisture dynamics using ERT, some used the Dipole-Dipole configuration on account of its improved resolution of vertical variations (Zeng et al., 2016; Greer et al., 2017), while others used the Wenner configuration to account for the horizontal structures (Hojat et al., 2019). Resistivity results are not unique using different measurements or representation, which is a very important source of uncertainty in data interpretation (Giudici, 2000; Clément et al., 2014). Some papers dealt with the depth of investigation (Oldenburg and Li, 1999; Robinson et al., 2012; Carey et al., 2019), and some with the sensitivity (Holbrook et al., 2014) of the resistivity image resulting from different electrode arrays. Ain-Lhout et al. (2016) focused on the ability to recognize resistivity differences in different media, and concluded that the Wenner configuration seems to be the most appropriate as it can differentiate the resistivities of the soil, soil moisture, and argan roots. These studies reported different perspectives to decide electrode arrays for more reliable and representative ERT measurements, and no similar study evaluated the ERT configuration performance by R^2 of the petrophysical relationship between resistivity and water content, especially in the forested site.

Here, two-dimensional ERT surveys were coupled with the SP method to characterize the infiltration process in response to rainfall at a resolution of decimeters, at the Nandadish experimental catchment between the Yangtze River and Huai River of eastern China. We also present observations of soil structure and root characteristics at 2 m deepth to assess the impact of structure on water flow processes. Meanwhile, TDR sensors are used to obtain the volumetric water content as an accurate reference to interpret the variation in the electrical resistivity as a function of soil water. The site-specific resistivity and soil water content (SWC, ρ–θ) relationships were developed based on a variety of ERT

https://doi.org/10.5194/hess-2023-190
Preprint. Discussion started: 29 August 2023

Hydrology and Earth System Sciences
Discussions

measuring configurations. This provided a more detailed description of the subsurface hydrologic response through quantitative comparison. And, unlike the single configuration such as Wenner or Dipole-Dipole that is commonly used, we used both configurations and compared them through the R^2 of the ρ–θ relationship to obtain the most appropriate measurement configuration for the soil moisture dynamics in response to rainfall at the study site.

The objectives of this study were (a) to investigate the potential of a combination of time-lapse ERT and SP for detecting the spatial-temporal variability of soil moisture dynamics in response to the rainfall at the forest field scale. (b) to evaluate the influence of different measuring configuration on the interpretation of resistivity data results, and quantify and visualize subsurface hydrological processes based on the established petrophysical relationship between resistivity and water content, using a spatial ERT and a conventional TDR method. (c) to evaluate the influence of vegetation root systems and subsurface structure on spatial soil moisture patterns and dynamics during the rainfall event by coupling structure and process descriptions. The datasets generated in this paper provide quantitative information on soil moisture dynamics in temporal and spatial dimensions that can improve the understanding of subsurface flow movements during rainfall in the forest field.

2 Methods

2.1 Study area

The study area, the Nandadish catchment with an area of 7897 m^2, was an experimental catchment belonging to the Chuzhou Scientific Hydrology Laboratory of the Nanjing Hydraulic Research Institute (118°12′37″ E, 32°17′24″ N). The Nandadish catchment is located at a typical climate transition zone (between the Yangtze River and Huai River Basin) from subtropical to the warm temperate of eastern China (Figure 1), with an average annual rainfall (from 1951 to 2016) of 1008 mm. Rainfall is strongly seasonal, with more than 80% of the total rainfall occurring from May to October.

https://doi.org/10.5194/hess-2023-190
Preprint. Discussion started: 29 August 2023

Hydrology and Earth System Sciences
Discussions
Open Access
EGU

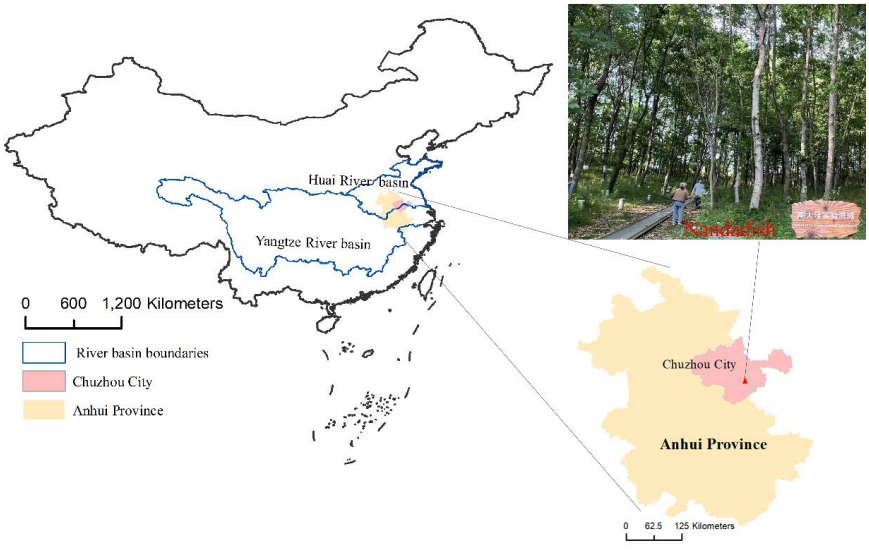

Figure 1: Location of the Nandadish site in the climate transition zone from subtropical to warm temperate, eastern China.

The upper part of the Nandadish is forested with a stand density of 1128 trees/ha; the substrate is Mesozoic andesite; the middle part is a loose Quaternary deposit varying from 0.5 to 7.0 m. Its perimeter is separated from the surrounding area by concrete boundary walls and acts as a watershed, making the Nandadish available as a forested critical zone experimental body suitable for hydrological research (Gu et al., 2018). As a typical area of deciduous broadleaved forest, the vegetation in the Nandadish is dominated by Quercus acutissima Carruth. and Broussonetia papyrifera, which account for 67.4% and 21.5% of the basal area, respectively.

Table 1: The Nandadish soil texture in the different locations and depths.

Pits Location	Depth (cm)	Clay % <2 μm	Silt % 2 to 50 μm	Sand % 50 to 2000 μm
	5	11.00	82.74	6.26
	15	11.62	82.95	5.43
	25	11.96	83.02	5.02
Toe	35	12.22	82.74	5.04
	55	13.32	80.87	5.81
	75	12.81	80.45	6.75
	105	14.32	79.65	6.03
Middle	5	13.16	58.64	28.20

https://doi.org/10.5194/hess-2023-190
Preprint. Discussion started: 29 August 2023

	15	9.50	47.27	43.24
	5	12.63	82.31	5.06
	15	11.43	84.01	4.56
	25	12.65	83.07	4.29
Top	35	12.15	83.89	3.97
	55	12.20	83.75	4.06
	75	12.41	83.29	4.30
	105	12.56	83.03	4.41

Soil properties analyses were conducted on samples collected from the top, middle, and the toe exploring pits (distributed at 7 m, 25 m and 45 m from the toe of the slope to the top) of a two-dimensional section in the Nandadish (Figure 2), at seven depths of 5, 15, 25, 35, 55, 75, and 105 cm. Three textural fractions, clay (0 to 2 µm), silt (2 to 50 µm), and sand (50 to 2000 µm), were used according to the United States Department of Agriculture (USDA) standards (Cassiani et al., 2015). The soil was uniform in the upper 1.05 m, consisting of a silt loam texture (Table 1), and the mean organic carbon was 10.31 g/kg.

The northwest hydrographic slope of the Nandadish crossed a transect of tree roots and open ground (Figure 2). The two-dimensional ERT system, SP electrodes, and the exploring pits were installed on the slope. Three exploring pits were excavated to facilitate the TDR installation and soil sampling The two-dimensional ERT system we installed consists of 100 stainless steel electrodes, 39 cm in length and 1 cm in diameter, inserted in the ground at a depth of 15 cm and spaced at a 0.5 m horizontal intervals along the slope (Figure 2). The total length of the surface ERT line was 49.5 m. The relative elevation of each electrode point was measured using a gradiometer and incorporated into the inversion processes. SP measurements in this paper were performed along the section that were nearly parallel to the 2-D ERT section, using Pb-$PbCl_2$ non-polarizing electrodes (developed by China University of Mining and Technology, Wang et al., 2022). The distance between the SP electrodes was 2 m, and the total length of the SP line was 38 m. SP electrodes along the slope were installed out at a depth of approximately 15 cm. Meanwhile, we also placed SP electrodes at depths of 5, 15, 25, 35, 55, 75, and 105 cm in the pit position, focusing on monitoring the infiltration processes. On this slope, the obvious surface roots were distributed at 25 to 26 (about 12 m) and 67 to 69 (about 33 m) ERT electrodes from the toe of the slope to the top.

https://doi.org/10.5194/hess-2023-190
Preprint. Discussion started: 29 August 2023

Hydrology and Earth System Sciences
Discussions
Open Access
EGU

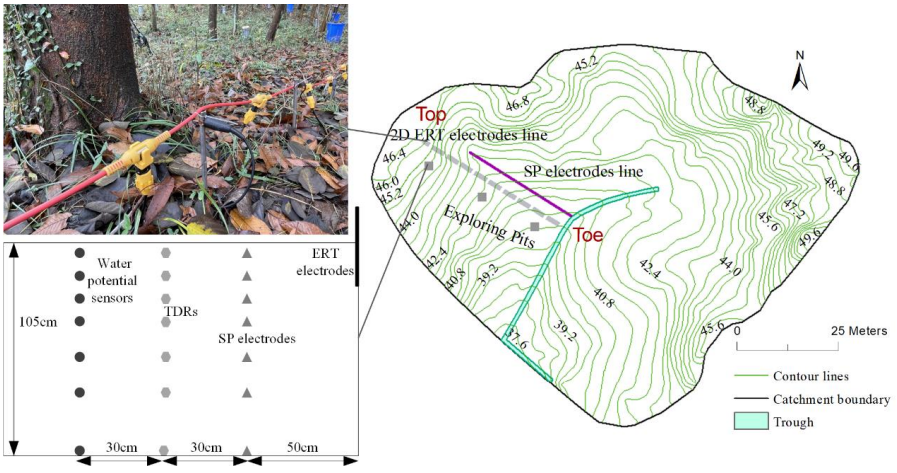

Figure 2: Experimental setup of the slope at the Nandadish site, including the location of ERT electrodes, SP electrodes, TDRs and water potential sensors.

2.2 Electrical resistivity tomography

2.2.1 Data acquisition and processing

The repeated (so called time-lapse) ERT surveys were carried out with the above-mentioned equipment every two weeks from June to October 2022. The measurements were intensified during rainy periods to better represent the rainfall infiltration processes in the subsurface. ERT data were collected using a GD-20 instrument (ST Geomative Co., Ltd, China), which is a multi-channel system for performing ERT, SP and Induced Polarization (IP) measurements. Meanwhile, the GD-20 was equipped with real-time online field monitoring mode to conduct unattended and automated surveys remotely for long periods.

In this work, two different four-pole configurations, Wenner and Dipole-Dipole array, were used for the acquisition of apparent electrical resistivity. Prior each measurement, a contact resistance test between the electrode and the soil was performed to verify the correct operation of the GD-20 monitoring system (Luongo et al., 2012; Zeng et al., 2016). Meanwhile, to avoid anomalies in the resistance measurements during drought caused by poor contact (dry soils can produce a vacuum at the soil-root interface), a little water was added to slightly wet the soil around the electrodes. Each measurement included 1370 measurement points for the Wenner and 1702 points for the Dipole-Dipole, and took approximately 40 minutes and 45 minutes, respectively.

https://doi.org/10.5194/hess-2023-190
Preprint. Discussion started: 29 August 2023

Hydrology and Earth System Sciences
Discussions

While it was not possible to collect reciprocals (current electrodes and potential electrodes are swapped) to determine the fast flow process (Guo et al., 2020), all ERT surveys included only the acquisition data of the direct measurement. After the surveys, all the apparent resistivity data from the ERT measurements were preprocessed to remove noisy data with anomalously high contact resistance (>5000 Ω) (Fan et al., 2020; Vanella et al., 2018).

The different soil temperature between deep soil layers of 105 cm and surface soil layers of 5 cm is 0 to 15.3°C during the study period. Each pixel of the above filtered apparent electrical resistivity was corrected for the effect of temperature referenced to 18°C using the following relationship (Amato et al., 2008; Srayeddin and Doussan, 2009).

$$\rho_T = \rho_{T_0}[1+\lambda(T_0 - T)] \quad (1)$$

where ρ_T is electrical resistivity (Ω m) at the temperature T (°C); ρ_{T_0} is electrical resistivity (Ω m) at the temperature T_0 (°C), T_0 = 18°C. λ is the temperature correction coefficient, $\lambda = 0.02$.

2.2.2 Data inversion

The true spatial distribution of resistivity can be determined by inversion of the subsurface apparent resistivity within a specified error level and appropriate inversion model constraints (Travelletti et al., 2012; Consoli et al., 2017). To process the time-lapse resistivity data, we used the 2D inversion software EarthImager, developed by Advanced Geosciences Inc., United States. The underdetermined and ill-posed nature of 2D resistivity inverse problems makes the inverse solution inherently nonunique. Additional constraints, or regularization, must be imposed on the model to extract an optimal solution. In this paper, the inversion is performed using a weighted least-squares approach with smoothness constraint (deGroot-Hedlin et al., 1990; Nimmer et al., 2007; AGI 2009). The resistivity distribution is solved by minimizing the objective function as seen below.

$$\mathbf{\Phi(m)} = [\mathbf{d} - f(\mathbf{m})]^T \mathbf{W}_d [\mathbf{d} - f(\mathbf{m})] + \alpha \mathbf{m}^T \mathbf{R} \mathbf{m} \quad (2)$$

where $\mathbf{m}$ is the model vector of resistivities, $\mathbf{m} = \log_e\left(\boldsymbol{\rho}^{-1}\right)$; $\mathbf{d}$ is the vector of measured resistance data; $f(\mathbf{m})$ is the forward model resistances (the forward operator); T is the matrix transfer; $\mathbf{W}_d$ is an error weighting matrix, i.e., measurement errors, quantified here using a certain percentage of noise as the data

https://doi.org/10.5194/hess-2023-190
Preprint. Discussion started: 29 August 2023

Hydrology and Earth System Sciences
Discussions

weight of 3%. α is a Lagrange multiplier and a stabilizing factor. It determines the amount of model roughness imposed on the model during the inversion. **R** is a roughness operator used to smooth the resistivity distribution and stabilize the inverse solution. The root mean square (RMS) in each survey was calculated to find a resistivity model whose response best fits the measured data (Tsai et al., 2021). An iterative solution is reached when the RMS error in percent is less than 5%.

The effect of soil characteristics, such as clay content, on the measured electrical resistivity should be minimized by accounting for differences in resistivity (Srayeddin and Doussan, 2009). To better identify the changes of wetting peaks due to rainfall, we need to select the base (pre-rainfall) resistivity dataset, which can be regarded as an a-priori resistivity model. The time-lapse inversion method was used to invert the difference between the monitor and base datasets. Instead of inverting the monitor dataset alone, the coherent inversion artifacts caused by numerical inaccuracies can be eliminated in the images. The result of the time-lapse inversion is presented as the percent change in resistivity between the two resistivity distribution. The resistivity change was calculated as the relative resistivity difference ($\Delta\rho$, %) (Luongo et al., 2012; Clément et al., 2014) between the monitor (ρ_i , Ω m) and the base data resistivity (ρ_0 , Ω m). An increase in resistivity results in a positive percent change and a decrease results in a negative percent change.

$$\Delta\rho = \frac{\rho_i - \rho_0}{\rho_0} \times 100 \quad (3)$$

2.3 Self potential

SP is a passive geophysical technique that uses a pair of non-polarizing electrodes and a high-impedance voltmeter to detect voltage differences caused by naturally occurring electrical currents. One source of electric current is associated with the flow of water in the subsurface through a permeable or porous material, also called the streaming potential. This current contribution originates from the polar water molecules moving through charged grain surfaces at the fluid-grain interface (Linde et al., 2011; Voytek et al., 2016). Therefore, there is a strong interest to obtain information relative to the fluid flow pattern using a SP method (Sidle et al., 2001; Suski et al., 2006). The depth of investigation for SP is difficult to determine because it depends on the strength of the current source (Voytek et al., 2016). The principle

https://doi.org/10.5194/hess-2023-190
Preprint. Discussion started: 29 August 2023


Hydrology and Earth System Sciences
Discussions

of SP can be described by the Ohm's law and Maxwell's equations as follows (Richards et al., 2010; Linde et al., 2011; Voytek et al., 2019).

$$j = \sigma E + j_s \quad (4)$$

$$\nabla \cdot j = 0 \quad (5)$$

where j is the total current density (Am^{-2}); σE is the conduction current density; σ is the electrical conductivity (Sm^{-1}); E is the electrical field (Vm^{-1}), and $E = -\nabla V$, V is the electrical potential between a reference and a potential electrode from SP method; and j_s is the source current density (Am^{-2}), generated by water movement or other possible current sources. These two equations can help obtained the distribution of V given knowledge of j_s.

ERT is sensitive to static or state variables such as water content, while SP is sensitive to dynamic processes such as water flow. For this reason, SP signals can be used to describe the water flow path in hydrology, and measured SP voltages should increase in the direction of flow (Voytek et al., 2019). Rather than one dimensional flow in horizontal (Linde et al., 2011; Voytek et al., 2016) or depth (Doussan et al., 2002), we used SP to evaluate both the two-dimensional soil water movement in this paper. The reference electrode was buried at a depth of approximately 60 cm and located 9 m from the center of the SP section, and the potential difference between the measurement and reference electrodes was recorded with a data collector (DataTaker 85, Biolab, Inc., Australia) at 1 min intervals.

Due to telluric currents and induction effects in the cables, many spikes occur in the time series of the SP data. The spikes in the time series were removed while maintaining the total amplitude of the SP variations. The temperature drift of the SP electrodes is very small, 0.01 mV/°C, So the effect of the offset due to temperature can be ignored (Wang et al., 2022).

2.4 Hydrometric and seismic prospecting

Rainfall data were collected from a cluster of tipping bucket rain gauges with the measurement error ≤ ±4% located at the automatic weather station 300 m away the Nandadish forest from June to October 2022. These rainfall data were collected at 1 minute intervals.

The soil water content (SWC) was monitored using a set of TDR probes (TDR315H, Acclima, Inc., United States). The probes were installed at the toe, middle and top of the slope where the electrical resistivity measuring electrodes were placed, horizontally at seven depths of 5, 15, 25, 35, 55, 75, 105

https://doi.org/10.5194/hess-2023-190
Preprint. Discussion started: 29 August 2023


Hydrology and Earth System Sciences
Discussions

cm in the subsurface. In the middle, as the depth of the bedrock from the ground surface is about 15 cm, only two probes were installed at the depths corresponding to 5 and 15 cm. The soil temperature can also be obtained from the TDR probes, which was required for the temperature correction of the electrical resistivity to a standard temperature. Water potentials were monitored at the same depths as the TDR sensors using Campbell 253 (Campbell 253, Campbell Scientific, Inc., United States). The SWC, soil temperature, and water potentials for each location were collected using a CR1000X data logger at 10 min intervals. All sensors were left in place for two weeks to ensure good contact with the surrounding soil.

The seismic refraction method was used to create the primary p-wave velocity and obtain the thickness information of weathering layers and the position of the fractured bedrock. The energy from a seismic source travels through the soil in the subsurface and is refracted when it reaches the transition of different material compositions and compaction. The seismic refraction data were recorded between the ERT and SP section using MCSEIS-SX48 (OYO Corporation, Japan) with 24 channel seismographs and 28 Hz vertical component geophones spaced at 2.0 m. The last geophone of the previous spread (48 m) became the first geophone of the next spread, this multiple spread allowed 49.5 m spread lengths. The shot was a 5 kg sledgehammer that struck a stainless-steel circular plate with a diameter of 10 cm and a thickness of 4 cm. The first arrival times of the P wave were picked manually on all traces. Based on a 2D layered velocity, the inversion was performed until the root-mean-square (RMS) error between the observed and modeled travel times reached 5 %. The inversion results are smooth boundaries with different velocity values. The 0.5 km s^{-1} contour on all final velocity models was used to delineate the transition between loose, highly porous media and the underlying saprolite, and the 1.2 km s^{-1} contour represents the transition between the saprolite and fractured bedrock (Holbrook et al., 2014; Carey et al., 2019).

https://doi.org/10.5194/hess-2023-190
Preprint. Discussion started: 29 August 2023

Hydrology and Earth System Sciences
Discussions

3 Results

3.1 Hydrometric observations

Rainfall during the flood season from June to October is shown in Figure 3. The rainfall that occurred on July 4, 2022 and produced a total rainfall of 133.5 mm within 2.6 hours was selected to analyze the infiltration behavior before, during, and after the rainfall event.

The changes in typical SWC and water potential of the different vertical soil layers were obtained by averaging of the same layer from pit 1 and pit 3. The SWC remained between 0.18 and 0.45 cm^3cm^{-3}, while water potential remained between 0 and -488 kPa during the study period. During the period without rainfall, the soil moisture and water potential measured at different depths decreased steadily. Peaks of the SWC and water potential generally coincided with rainfall events, with the response typically attenuated at deeper soil depths. For example, with the rainfall on August 26, 2022, the SWC and water potential showed an expected increasing tendency in varying degrees only at the near-surface depths of 5, 15, and 25 cm, while there was no significant response at other depths. In addition, the near-surface sensors at 5, 15, and 25 cm depths recorded a lower SWC values than those at the greater depths throughout the flood season, as the top soils dried out due to root water uptake and soil evaporation in forested areas.

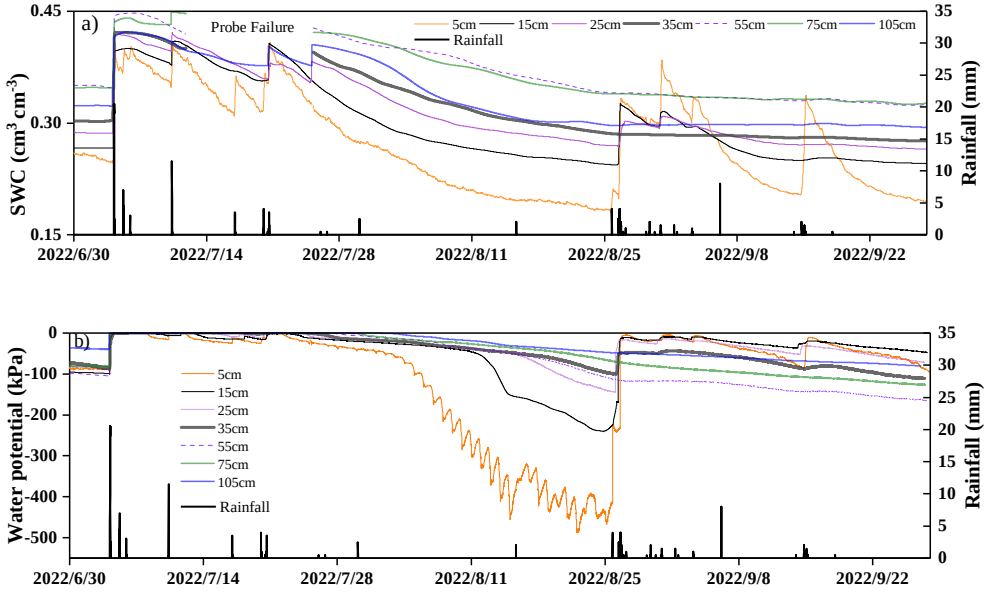

https://doi.org/10.5194/hess-2023-190
Preprint. Discussion started: 29 August 2023

Hydrology and Earth System Sciences
Discussions
Open Access
EGU

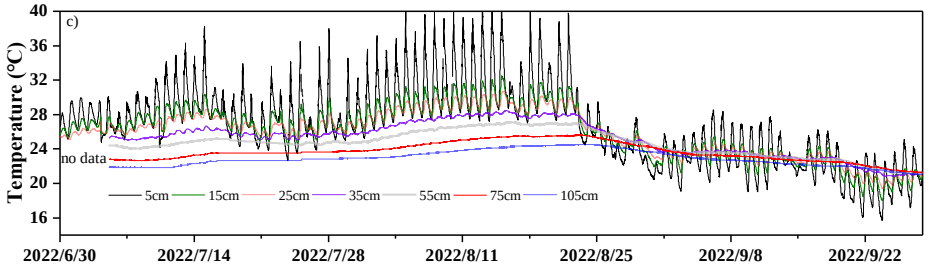

Figure 3: Precipitation, water content, water potential, and soil temperature variation from June to October 2022 at the study site.

During the flood season, the minimum and maximum soil temperatures in the soil layer above 105 cm were 16℃ and 42℃, respectively. Soil temperatures showed a significant decrease after the end of August. Spatially, soil temperature varied significantly near the surface, and the amplitude and range of variation decreased with depth. A similarly sinusoidal daily variation of soil temperature was also observed near the surface at 5, 15, 25, and 35 cm, with the highest temperature of the day being reached at around 12:00-14:00.

3.2 Soil Moisture changes response to precipitation

3.2.1 Spatial variation of soil electrical resistivity

The resistivity changes are analyzed for the typical rain event that occurred on July 4, 2022. The mean SWC of 2 days before this rain event in the soil layer above 105 cm was 0.31 cm^3cm^{-3}. The mean inverted resistivity obtained for each ERT measurement in Figure 4a presents a decreasing trend during rainfall events, from 25.8 to 22.0 Ω m . The resistivity data were corrected based on temperature, so we can reasonably relate this decrease in resistivity to an increase in water content from rainfall infiltration (Travelletti et al., 2012; Greer et al., 2017), assuming no change in the subsurface geologic structure. Four ERT tomograms, shown in Table 2 and Figure 4b, were used to analyze the differential resistivity before, during, and after rainfall. The time-lapse ERT was taken from July 4, 17:35 (35 min after rainfall) to July 5, 08:00 (15 h after rainfall). At 35 min after rainfall (Figure 4b, Tomogram 1), the water content monitored by TDRs in pit 1 and pit 3 was 0.35 and 0.39 cm^3cm^{-3}, respectively. The lower resistivity at 30 to 49.5 m and the higher resistivity at 0 to 29 m in the subsurface were detected, indicating the initial higher and lower water content, respectively.

https://doi.org/10.5194/hess-2023-190
Preprint. Discussion started: 29 August 2023

Hydrology and Earth System Sciences
Discussions

308 **Table 2: Summary of ERT inversion before, during, and after rainfall.**

ERT Survey time	No. of Total measurements	No. of rejected measurements	No. of iterations	RMS (%)
Tomogram 1, 35 min after rainfall	1702	71	6	4.71
Tomogram 2, 140 min after rainfall	1689	250	8	4.29
Tomogram 3, 210 min after rainfall	1688	283	8	4.16
Tomogram 4, 15 h after rainfall	1700	205	4	3.48

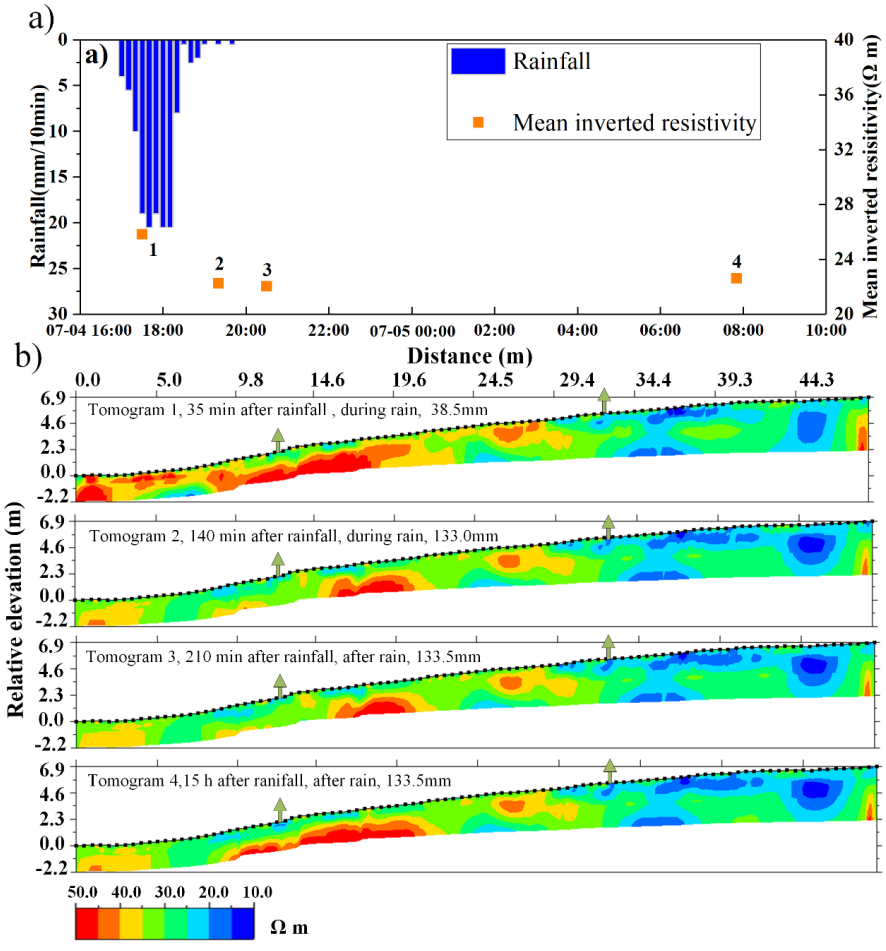

309
310 **Figure 4: ERT monitoring during the rainfall event, with a) Evolution of mean inverted resistivity during**
311 **ERT monitoring versus rain, b) the differenced resistivity model processed before, during, and after rainfall.**

312 Figure 5 shows that 140 minutes after rainfall, a total rainfall of 133.0 mm caused up to a maximum
313 76% decrease in resistivity at 0 to 20 m horizontally, 0 to 2.2 m depth (2.2 m is the depth of investigation,
314 and structures below this depth cannot be used for geological interpretation). Meanwhile, the water
315 content in each soil layer above 105 cm reached more than 0.40 cm^3cm^{-3}, with the average moisture

https://doi.org/10.5194/hess-2023-190
Preprint. Discussion started: 29 August 2023

Hydrology and Earth System Sciences
Discussions

content in pit 1 and pit 3 being 0.42 and 0.43 cm^3cm^{-3}, respectively. The significant decrease in resistivity was concentrated at the toe of the slope rather than the top, which may be attributed to rapid ponding of water caused along the slope. In addition, the site with lower initial water content and its silt loam texture would result in a more pronounced change rate of resistivity change. After 210 minutes, the rain almost stopped and the size of the subsurface accumulation area (blue) no longer increase significantly, but its degree of decreased resistivity and the increase in water content continually increased. At this moment, the average soil moisture in pit 1 and pit 3 were 0.43 and 0.44 cm^3cm^{-3}, respectively, both increased by 0.01 cm^3cm^{-3} compared to the water content at 140 minutes after rainfall. As shown in Figure 5, the 10% change in resistivity between Tomograms 2 and 3 indicated that water preferentially reached deeper storage zones through the high permeability zones (blue). Meanwhile, the high permeability zones quickly became high resistivity areas (red) after the 15 hours (the average water content in pit 1 and pit 3 were 0.41 and 0.42 cm^3cm^{-3}, respectively). These separate preferential flow paths stimulated by high rainfall intensity, were likely the large voids such as the weathered or fractured rock that could easily move the wet peak during rainfall. Note that the resistivity increases (red or yellow) during precipitation in Figure 5, which is not an unreasonable response to the adding of water in the subsurface. This may be due to the inversion artifacts rather than a true increase in resistivity during the inversion process (Greer et al., 2017).

https://doi.org/10.5194/hess-2023-190
Preprint. Discussion started: 29 August 2023

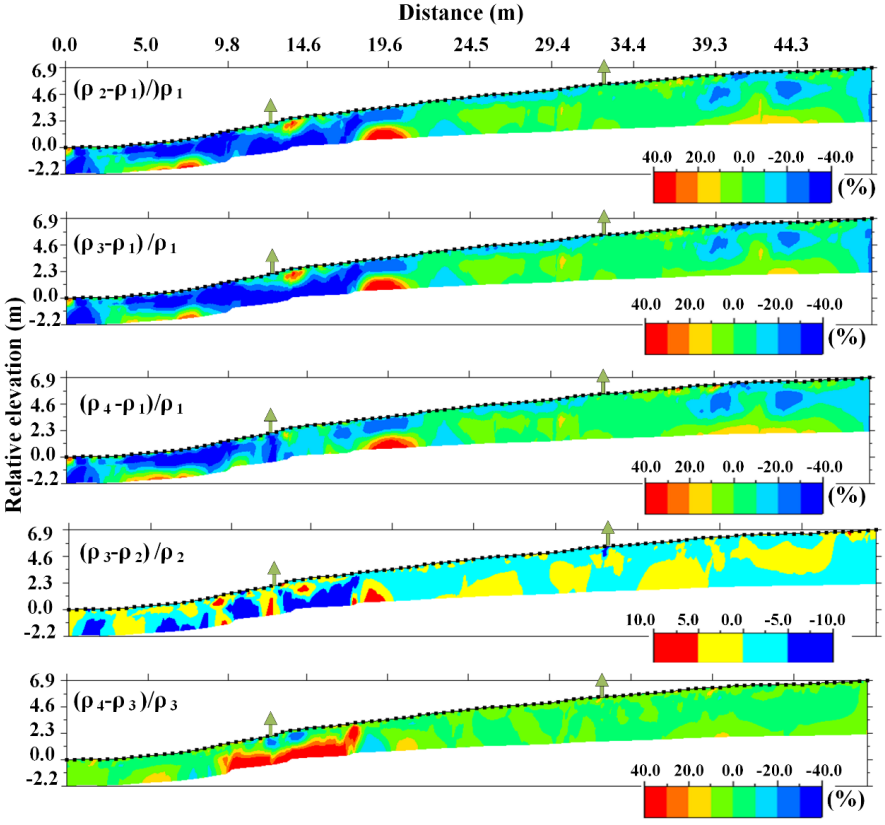

Figure 5: Percentage change in resistivity from different initial model (The first three figures are the percentage changes of resistivity with tomogram 1 as a background, and the next two figures are the percentage changes of resistivity measured at adjacent times).

3.2.2 Quantitative comparison between Soil Moisture and Resistivity

SWC variation is considered to be the most influential parameter for resistivity when the temperature variation is compensated and other factors such as solid constituents remain stable (Clément et al., 2014). Resistivity always links to water content through Archie's law (Archie, 1942; Garré et al., 2011; Tsai et al., 2021) which assumes the clay content is negligible. Whereas in the study area clay content is usually greater than 10%. This condition cannot be considered satisfied. Referring to Travelletti et al. (2012) and (Fan et al., 2015), we directly used a power-law fit in this paper. To map an observed subsurface hydrological response, we developed site-specific resistivity and SWC (ρ–θ) relationships by coupling water content from TDR probes at seven depths with ERT voxels at the corresponding positions. Six ERT surveys using Wenner and Dipole-Dipole respectively, along with TDR measurements, are

https://doi.org/10.5194/hess-2023-190
Preprint. Discussion started: 29 August 2023

Hydrology and Earth System Sciences
Discussions
Open Access
EGU

available for the same position of different pits and probe depths, which are pooled together as soil conditions were similar. Thus, we established relationships for two configurations (Wenner and Dipole-Dipole) during the flood season. As shown in Figure 6, the ρ-θ relationships are negatively correlated to a greater or lesser extent. Note that ρ and θ varied between 18.8 and 49.7 Ω m, and 0.25 and 0.44 cm^3cm^{-3}, respectively. For the Dipole-Dipole (R^2 = 0.80), the relationship appears much more concentrated than for the Wenner (R^2 = 0.70). A better power fit was obtained using the Dipole-Dipole in this paper.

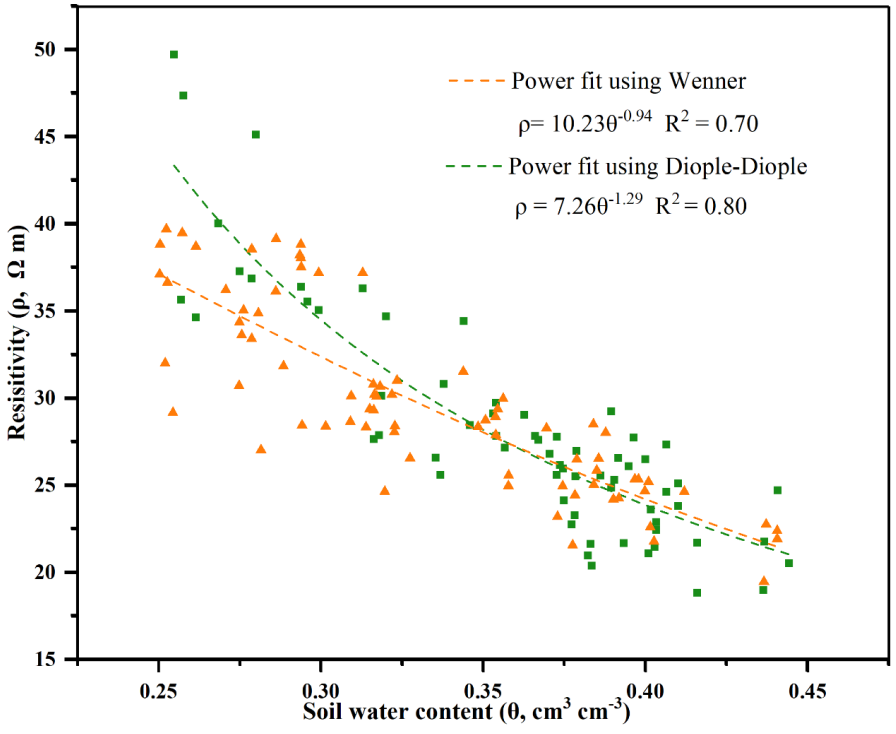

Figure 6: The ρ–θ relationship fitted with a power function with Dipole-Dipole or Wenner.

3.2.3 2D images of soil moisture variation

The spatial variation of soil electrical resistivity cannot be used to directly provide quantitative estimates of the hydrological process. Therefore, based on the site-specific ρ–θ relationship proposed in the study area, 2-D images of SWC variation during the rainfall event were obtained. As shown in Figure 7, high SWC occurred at the top of the hillslope, and decreased rapidly down the slope. There are two preferential flow paths along the soil transect, as indicated by the red arrow. Combined with the seismic wave velocity results, the left preferential flow was connected through the soil-highly fractured bedrock interface,

https://doi.org/10.5194/hess-2023-190
Preprint. Discussion started: 29 August 2023

Hydrology and Earth System Sciences
Discussions
Open Access
EGU

which could be rapidly invaded by water. The right indicated the possible presence of a more permeable saprolite. In addition, the location of the Quercus acutissima Carruth site (the green arrow on the left) became wetter during the rainfall infiltration phase (during rainfall) and the rainfall distribution phase (after rainfall). In contrast, Broussonetia papyrifera site (the green arrow on the right) showed no visible change in wetness. This phenomenon may reflect the regulation of tree species and their root distribution characteristics for the movement of water flow. Unlike Broussonetia papyrifera with its shallow root system, Quercus acutissima Carruth with its deeper roots may take longer to receive the available water flow in the deeper soil layers and have a more pronounced effect on soil moisture changes.

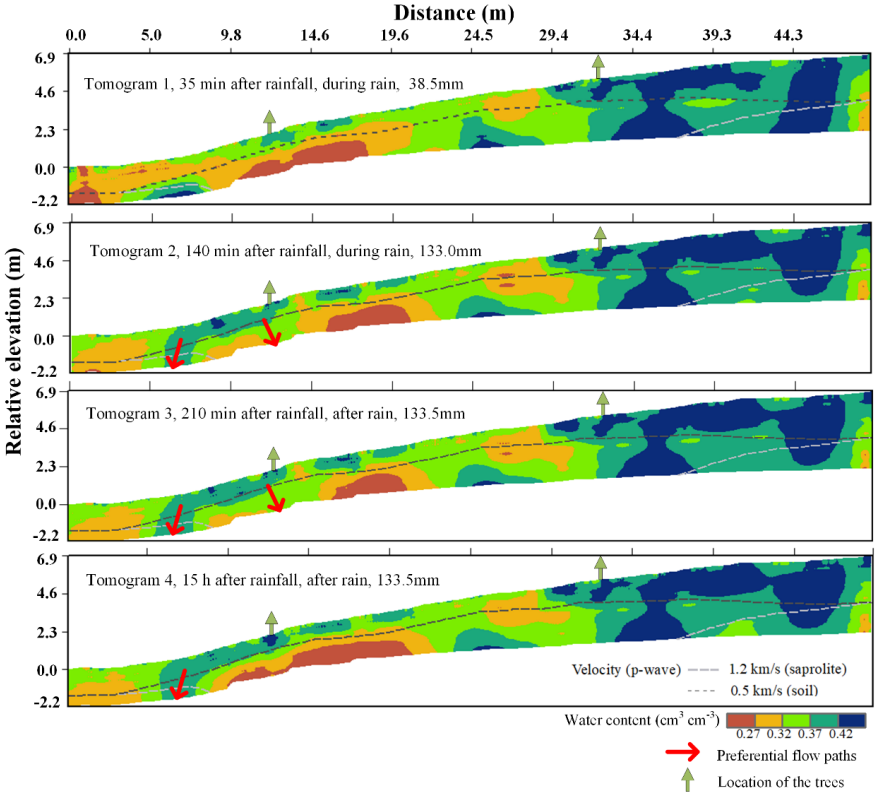

Figure 7: 2D images of SWC variation in the soil layer, estimated from the *ρ*–*θ* relationship relationship. The green arrow on the left is the location of the Quercus acutissima Carruth and the right is the Broussonetia papyrifera.

https://doi.org/10.5194/hess-2023-190
Preprint. Discussion started: 29 August 2023

Hydrology and Earth System Sciences
Discussions

3.3 Direction of water movement

Figure 8a shows the SP variability at depths corresponding to the rainfall. The typical rain event on July 4, 2022 resulted in an increase and positive SP signal at different depths. The SP increase at 15, 25, 35 and 55 cm depths occurred at 7, 17, 26, and 32 min after the rainfall. The response of SP near the surface soil layers is more rapid, and the response time is delayed with the increasing depth. In addition, as shown in Table 3, the rainfall caused an increase in the amplitude of the SP signal at a 15 cm depth with 7.5 mV, which is more significant than in the 25 cm soil layers with an increase of 5.0 mV. Meanwhile, the increase in SP amplitude at 35 cm depth was 11.4 mV, which is the maximum increase in SP amplitude at depth. Apparently, the increase in SP amplitude does not always increase with depth.

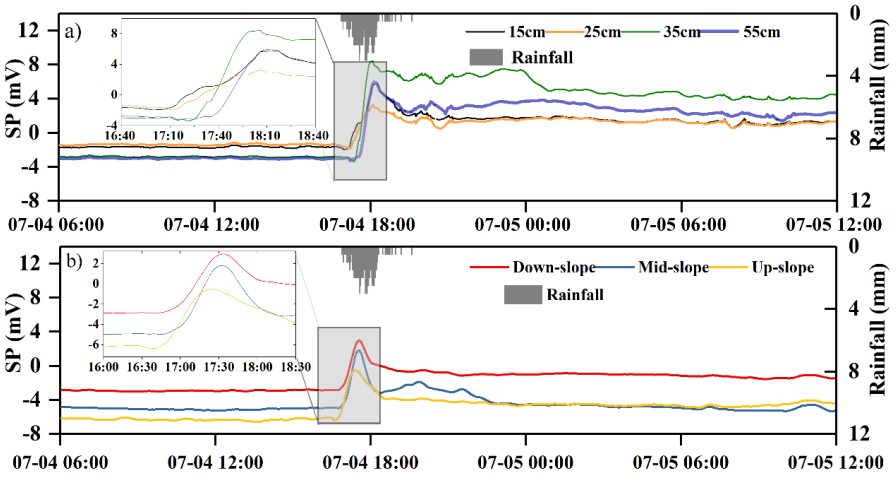

Figure 8: Response of the SP signal to rainfall a) in the vertical depths, and b) in the horizontal direction along the slope.

To depict the lateral water movement, we divided the SP data into up-slope, mid-slope, and down-slope by averaging every six available data except for the first electrode (no data). As shown in Figure 8b and Table 3, the SP signal on the up-slope, mid-slope, and down-slope started to show a response at 3, 3, and 4 min after rainfall, respectively. This faster response time could be attributed to the fact that all SP monitoring electrodes on the slope were installed at a depth of 15 cm, where they are more susceptible to infiltration of rain. The rainfall-induced SP amplitude increase was also high, and the maximum increase reached 7.0 mV. We can also observe the apparent fluctuating variations of SP after the rainfall, which is most likely related to the disturbance of continuous rainfall distribution.

https://doi.org/10.5194/hess-2023-190
Preprint. Discussion started: 29 August 2023

Hydrology and Earth System Sciences
Discussions
Open Access
EGU

Table 3: Variation of the SP due to the rainfall in the vertical depth and the horizontal position along the slope.

Location	SP electrode depth (cm)	Response time (min)	SP before rainfall (mV)	Max SP during rainfall (mV)	Rainfall-induced SP increase (mV)
Vertical Depths	15	7	-1.7	5.8	7.5
	25	17	-1.7	3.3	5.0
	35	26	-3.0	8.4	11.4
	55	32	-2.9	5.9	8.8
Down-slope	15	4	-2.7	3.2	5.9
Mid-slope	15	3	-4.7	2.3	7.0
Up-slope	15	3	-5.8	-0.6	5.2

Since the measured SP voltages should increase in the direction of water flow, this suggests that the water flow down the slope or into deeper soil layers should result in an increase in SP. As shown in Table 3, the largest increase of SP in the down-slope location indicates the presence of lateral subsurface flow. However, the magnitude changes between the slope locations are small. The difference between the largest magnitude caused by rainfall in the mid-slope and the up-slope locations is only 1.8 mV (7.0 less 5.2). In the vertical depths, the water flows to the 35 cm depth where the SP is maximum. The difference between the maximum SP of 25 cm and 35cm reached 6.4 mV (11.4 less 5.0), which is much larger than the maximum amplitude change of 1.8 mV from the lateral flow on the slope. Therefore, we concluded that the vertical infiltration flow plays a greater role than the lateral flow in the near-surface above 55 cm at the Nandadish site.

We proposed a refined conceptual model to represent the water movement in the study area (Figure 9). Precipitation rapidly infiltrated into the surface soil layer,and the vertical infiltration was significant in comparison to the lateral transmission flow. The water flow then continues to infiltrate along a more permeable saprolite before entering the fissures in the fractured bedrock. The fractured bedrock layer could be rapidly invaded by water, resulting in preferential infiltration along the lateral or vertical fissures. Once the water encounters the bedrock, a limited lateral flow may occur above the bedrock surface, and some water may infiltrate into the aquifer as deep drainage.

https://doi.org/10.5194/hess-2023-190
Preprint. Discussion started: 29 August 2023

Hydrology and Earth System Sciences
Discussions
Open Access
EGU

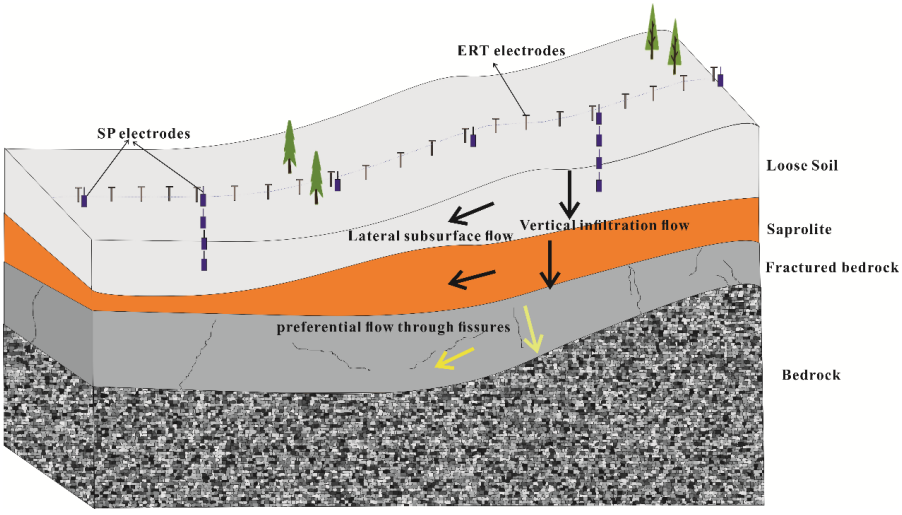

413
414 **Figure 9: The conceptual model to depict the water movement in the Nandadish site.**

415 **4 Discussion**

416 **4.1 Characterizing variation of subsurface flow using time-lapse ERT and SP**

417 The typical heavy rainfall in the study site resulted in a rapid water content response in the shallow soil
418 in a short time, as confirmed by the TDRs (Figure 3). However, the hydrological monitoring could not
419 provide further information to distinguish the infiltration pathways. Here, a combination of time-lapse
420 ERT and SP was presented. ERT allowed us to observe the evolution of the wetting peak under transient
421 unsaturated conditions with a sound spatial resolution, when rainfall occured over a fixed rainfall
422 simulator location (Carey et al., 2019). However, the natural rainfall often occurs over the entire slope,
423 making it difficult to use ERT alone to determine whether the wetting evolution is dominated by lateral
424 subsurface flow or vertical infiltration flow. Therefore, the SP data with a high temporal resolution of 1
425 min interval can be used to explain the evaluation. The two-dimensional (horizontal and depth) SP results
426 in Figure 8 show that the vertical flow rather than the lateral flow dominates, to drainage large amounts
427 of rainwater into the subsoil in the Nandadish forecast catchment. Preferential flow paths are common in
428 forest soils (Sidle et al., 2001; Dick et al., 2018). Two obvious vertical preferential flow paths in Figure
429 7 were observed using ERT, providing important vertical hydrological connections between deep and
430 shallow water during a rainfall event. The development of this combined approach provides the

https://doi.org/10.5194/hess-2023-190
Preprint. Discussion started: 29 August 2023

Hydrology and Earth System Sciences
Discussions
Open Access
EGU

opportunity for upward trends in moisture content and water flow direction, providing a earliest possible warning of runoff and landslide related to rainfall events, which could be extended to other regions.

Spatially, the resolution of the shallow (2.2 m) ERT inversion was improved by setting a smaller electrode distance (0.5 m). For temporal resolution, the data collection time with a frequency of 1 to 3 hours (a single acquisition takes 45 min) is suitable for monitoring the development of infiltrating water in the unsaturated situation. However, it is necessary to seek improvements in more frequent and faster acquisition equipment that will help improve the temporal resolution in the future research. Besides, mapping subsurface flow at multiple rainfall intensities and types could provide complementary and valuable information to characterize and locate water movements in the Nandadish catchment. This is of great interest for the development of hydrological forecasting models.

4.2 Influence of different ERT configuration on the interpretation of resistivity

The scatter (the larger R^2 of 0.80 in the whole periods) of the ρ–θ relationships using Dipole-Dipole is slightly better than Wenner in Figure 6. The robust agreement between ERT and the SWC from TDR indicates that the usefulness of ERT for the spatial estimation of subsurface flow dynamics in the forest site. Based on this, six additional ERT results measured with the Dipole-Dipole were used to verify the reliability of the proposed ρ–θ relationships in Figure 6 by an evaluating R^2 between the θ from TDR (θ-TDR) and θ from ERT using the ρ–θ relationship (θ-ERT). As presented in Figure 10, the verification results show that the R^2 coefficient was 0.78. These data demonstrate the robustness of the proposed ρ–θ relationship in practical applications, allowing interpretations of ρ in terms of hydrodynamic variations.

From a quantitative point of view by using the R^2 as a performance criterion, these results also suggest that in forested areas, the Dipole-Dipole may better help to obtain a more robust resistivity interpretation, when TDR was used to obtain the volumetric water content as an accurate reference. This may be attributed to the fact that the dipole-dipole array has better resolution for vertical structures such as the preferential flow induced by soil cracks (Zeng et al., 2016).

https://doi.org/10.5194/hess-2023-190
Preprint. Discussion started: 29 August 2023

Hydrology and Earth System Sciences
Discussions

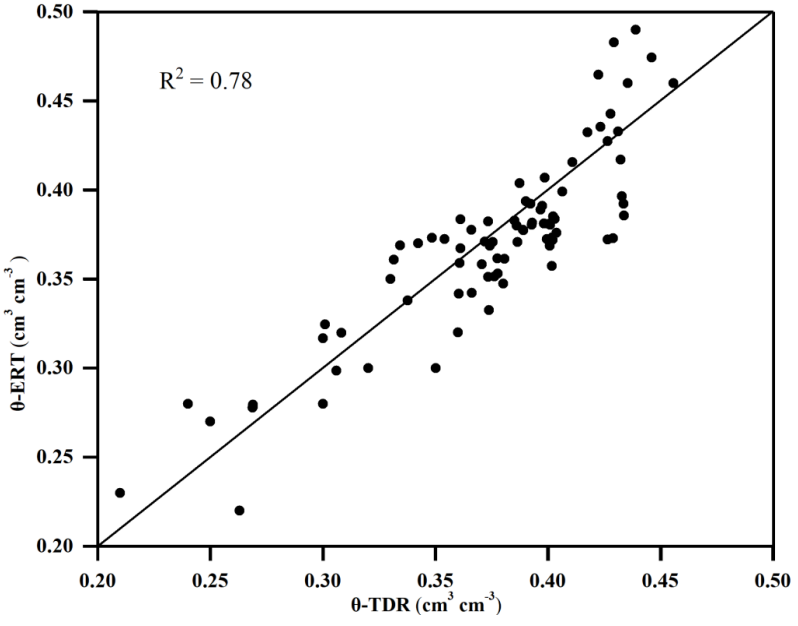

Figure 10: Comparison the SWC from ERT and the SWC from TDR to evaluate the robustness of the eatablished ρ–θ relationship.

4.3 Influence of root characteristics on the water infiltration

The infiltration process and soil moisture dynamics during a rainfall event as confirmed with higher heterogeneity in the resistivity and water content, were linked to the greater subsurface heterogeneity at the Nandadish catchment due to the distributed tree roots and shattered geological structure, both of which are known to be present at the forest site (Cassiani et al., 2015). At the tree root sites, the variation of water content at depth with typical rainfall processes were analyzed by converting the resistivity (Dipole-Dipole measurements) to water content distributions through the quantitative relationship established in this paper. Figure 11 shows an interesting phenomenon that tree species with different root structures can potentially lead to a differential distribution of water. The soil water content before the rainfall at the Quercus acutissima Carruth site was relatively small and drier than that of the Broussonetia papyrifera site, so the degree of change in water content due to rainfall was more pronounced, especially in the shallow surface layer. Generally, the amount of rainfall and the pre-soil condition together determine the degree of change of water content in the subsurface. At the site of Broussonetia papyrifera, the water content decreases with the depth, while at the site of Quercus acutissima Carruth, the trend is

https://doi.org/10.5194/hess-2023-190
Preprint. Discussion started: 29 August 2023

Hydrology and Earth System Sciences
Discussions
Open Access
EGU

exactly the opposite. The difference was more likely caused by the shallow roots of the Broussonetia papyrifera, which tended to retain more soil water at the surface. Instead, Quercus acutissima Carruth is expected to uptake and store water in the deeper depths. At the Quercus acutissima Carruth site, we found a significant and abrupt change in water content at the depth of 1.5 m. This may occur across boundaries of root and soil layers where root activity diverts new rainwater to replace the old and salty water. It is important to notice that deep and shallow root systems may also lead to an additional uncertainty in the estimation of the soil moisture content.

In this paper, we have made a two-dimensional explanation using the time-lapse ERT and SP, and found that the substructure and root distribution may directly affect the water content dynamics. Future studies will be directed toward a better understanding of how root characteristics affect the soil water content dynamics, by combining stem-centered 3-D surface and cross-hole ERT measurements with 3-D SP with short acquisition time.

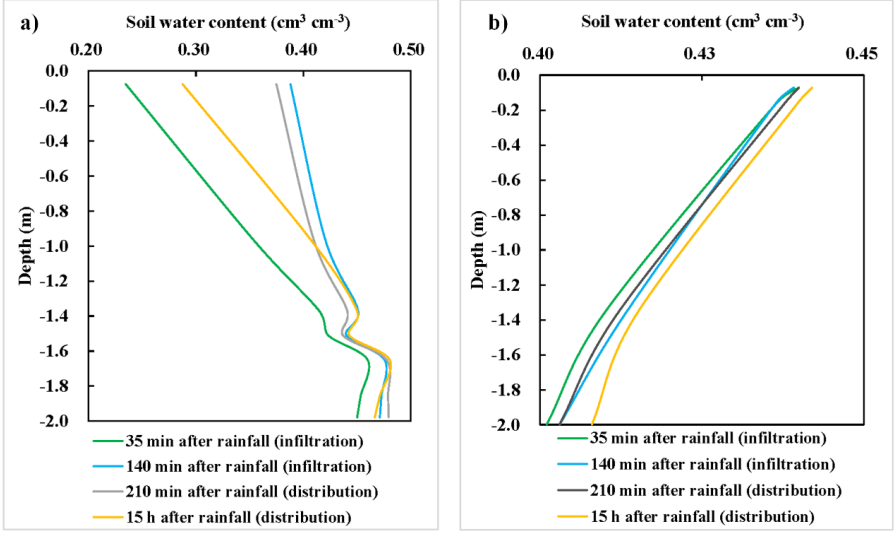

Figure 11: Depth profiles with tree locations from electrical resistivity tomography measurements during and after rainfall, with a) for the Quercus acutissima Carruth and b) for the Broussonetia papyrifera.

5 Conclusions

This study contributes a conjunctive utility of time-lapse ERT and SP methods to realize the detailed spatial-temporal measurements of soil moisture dynamics and the water movement direction during

https://doi.org/10.5194/hess-2023-190
Preprint. Discussion started: 29 August 2023


Hydrology and Earth System Sciences
Discussions

precipitation. This helps overcome the limitations of probe- or sample-based methods in terms of sample range or repeatability. Rather than simply describing the water status obtained by ERT, SP can assist in obtaining water flow information that has rarely been emphasized in previous studies. In addition, we developed site-specific ρ–θ relationships based on a variety of ERT measuring configurations and soil moisture conditions. This provided a more detailed description of the subsurface hydrologic response through quantitative comparison. Unlike the single configuration such as Wenner or Dipole-Dipole that is usually used, we used both configurations and compared them by the R^2 of the ρ–θ relationship to obtain the most appropriate measurement configuration. Moreover, information on underground structures obtained from seismic refraction was combined with the water flow processes due to rainfall, to improve the understanding of the fluid movement in the subsurface. Although some artifacts are difficult to resolve, the combined utility of time-lapse ERT and SP methods proved effective in interpreting moisture content development and their direction. The presence of trees with different root characteristics and heterogeneous structures will affect the infiltration and distribution process of rainfall in the soil. Major conclusions are summarized below.

(1) It is effective to apply the combination of time-lapse ERT and SP for subsurface flow dynamics during the rainfall. The results provided by the SP clearly showed that the difference between the largest magnitude caused by rainfall along the slope is only 1.8 mV. In the vertical depths, the difference between the maximum SP reached 6.4 mV, which is much larger than the maximum amplitude change of 1.8 mV from the lateral flow on the slope. Therefore, the vertical flow rather than lateral flow dominates, to drain large amounts of rainwater into the subsurface in the Nandadish forecast catchment. Obvious vertical preferential flow paths were observed using ERT, providing important vertical hydrological connections between deep and shallow water during a rainfall event.

(2) Based on the established site-specific resistivity and SWC (ρ–θ) relationships by coupling water content from TDR probes at depth with ERT voxels in the corresponding positions, we found that a better power fit was obtained using the Dipole-Dipole with $R^2 = 0.80$ than the Wenner with $R^2 = 0.70$. The Dipole-Dipole configuration may help obtain more robust resistivity interpretations in the forested areas.

(3) The infiltration process and soil water moisture dynamics during a rainfall event, as confirmed by higher heterogeneity in the resistivity, were affected by the distributed tree roots and the fractured

https://doi.org/10.5194/hess-2023-190
Preprint. Discussion started: 29 August 2023

Hydrology and Earth System Sciences
Discussions
Open Access
EGU

geological structure. The preferential flow were connected through the soil-highly fractured bedrock interface or permeable saprolite, which could be rapidly invaded by water. Trees with shallow roots tended to retain a greater water content at the surface. Deep-rooted trees absorb and store water in deeper layers, resulting in significant abrupt changes in the water content of the deeper soil layers. The large permeability changes such as preferential flow due to the land cover and characteristics should be incorporated into physical hydrological models, which will be useful for the further refinement of the infiltration mechanism and simulation model development.

Data Availability

Measured raw and inverted time-lapse ERT data are the property of the Chuzhou Scientific Hydrology Laboratory. These data are available from the corresponding author on request.

Authors Contribution

Supervision for this research were acquired by Jiufu Liu and Guodong Liu. The methodology, study conception and experiments were designed and performed by Aimin Liao and Wenhang Jiang. The instrument, software, and data collection were provided by Jiufu Liu and and Aimin Liao. The interpretation of results were handled mainly by Wenhang Jiang. Wenhang Jiang written and prepared the original manuscript with contributions from all co-authors.

Competing Interest

The authors declare that they have no conflict of interest.

Acknowledgements

This study was supported by Nation Nature Science Foundation of China (Grant No. 91847301, 92047203), the Science Foundation of Nanjing Hydraulic Research Institute (Y522017), and the Second Tibetan Plateau Scientific Expedition and Research (STEP) program (Grant No. 2019QZKK0203).

https://doi.org/10.5194/hess-2023-190
Preprint. Discussion started: 29 August 2023

References

Advanced Geosciences, Inc. (AGI). Instruction Manual for EarthImager 2D Version 2.4.0 Resistivity and IP Inversion Software. Advanced Geosciences, Inc. Austin, TX, USA.

Ain-Lhout, F., Boutaleb, S., Diaz-Barradas, M. C., Jauregui, J., and Zunzunegui, M.: Monitoring the evolution of soil moisture in root zone system of Argania spinosa using electrical resistivity imaging, Agric. Water Manag., 164, 158–166, https://doi.org/10.1016/j.agwat.2015.08.007, 2016.

Amato, M., Basso, B., Celano, G., Bitella, G., Morelli, G., and Rossi, R.: In situ detection of tree root distribution and biomass by multielectrode resistivity imaging, Tree Physiol., 28, 1441–1448, https://doi.org/10.1093/treephys/28.8.1441, 2008.

Archie, G. E.: The Electrical Resistivity Log as an Aid in Determining Some Reservoir Characteristics, Transactions of the AIME, 146, 54–62, https://doi.org/10.2118/942054-G, 1942.

Beff, L., Günther, T., Vandoorne, B., Couvreur, V., and Javaux, M.: Three-dimensional monitoring of soil water content in a maize field using Electrical Resistivity Tomography, Hydrol. Earth Syst. Sci., 17, 595–609, https://doi.org/10.5194/hess-17-595-2013, 2013.

Carey, A. M., Paige, G. B., Carr, B. J., Holbrook, W. S., and Miller, S. N.: Characterizing hydrological processes in a semiarid rangeland watershed: A hydrogeophysical approach, Hydrol. Process., 33, 759–774, https://doi.org/10.1002/hyp.13361, 2019.

Cassiani, G., Godio, A., Stocco, S., Villa, A., Deiana, R., Frattini, P., and Rossi, M.: Monitoring the hydrologic behaviour of a mountain slope via time-lapse electrical resistivity tomography, Near Surf. Geophys., 7, 475–486, https://doi.org/10.3997/1873-0604.2009013, 2009.

Cassiani, G., Boaga, J., Vanella, D., Perri, M. T., and Consoli, S.: Monitoring and modelling of soil–plant interactions: the joint use of ERT, sap flow and eddy covariance data to characterize the volume of an orange tree root zone, Hydrol. Earth Syst. Sci., 19, 2213–2225, https://doi.org/10.5194/hess-19-2213-2015, 2015.

Clément, R., Moreau, S., Henine, H., Guérin, A., Chaumont, C., and Tournebize, J.: On the value of combining surface and cross-borehole ERT measurements to study artificial tile drainage processes, Near Surf. Geophys., 12, 763–776, https://doi.org/10.3997/1873-0604.2014034, 2014.

https://doi.org/10.5194/hess-2023-190
Preprint. Discussion started: 29 August 2023

Consoli, S., Stagno, F., Vanella, D., Boaga, J., Cassiani, G., and Roccuzzo, G.: Partial root-zone drying irrigation in orange orchards: Effects on water use and crop production characteristics, Eur J Agron, 82, 190–202, https://doi.org/10.1016/j.eja.2016.11.001, 2017.

deGroot-Hedlin, C. and Constable, S.: Occam's inversion to generate smooth, two-dimensional models from magnetotelluric data, Geophysics, 55, 1613–1624, https://doi.org/10.1190/1.1442813, 1990.

Dick, J., Tetzlaff, D., Bradford, J., and Soulsby, C.: Using repeat electrical resistivity surveys to assess heterogeneity in soil moisture dynamics under contrasting vegetation types, J. Hydrol., 559, 684–697, https://doi.org/10.1016/j.jhydrol.2018.02.062, 2018.

Doussan, C., Jouniaux, L., and Thony, J.-L.: Variations of self-potential and unsaturated water flow with time in sandy loam and clay loam soils, J. Hydrol., 267, 173–185, https://doi.org/10.1016/S0022-1694(02)00148-8, 2002.

Fan, B., Liu, X., Zhu, Q., Qin, G., Li, J., Lin, H., and Guo, L.: Exploring the interplay between infiltration dynamics and Critical Zone structures with multiscale geophysical imaging: A review, Geoderma, 374, 114431, https://doi.org/10.1016/j.geoderma.2020.114431, 2020.

Fan, J., Scheuermann, A., Guyot, A., Baumgartl, T., and Lockington, D. A.: Quantifying spatiotemporal dynamics of root-zone soil water in a mixed forest on subtropical coastal sand dune using surface ERT and spatial TDR, J. Hydrol., 523, 475–488, https://doi.org/10.1016/j.jhydrol.2015.01.064, 2015.

Garré, S., Javaux, M., Vanderborght, J., Pagès, L., and Vereecken, H.: Three-Dimensional Electrical Resistivity Tomography to Monitor Root Zone Water Dynamics, Vadose Zone J, 10, 412–424, https://doi.org/10.2136/vzj2010.0079, 2011.

Giudici, M.: Fast representation of dipole-dipole geoelectrical data with pseudosections for regional surveys, Annals of Geophysics, 43(2). http://hdl.handle.net/2122/1263

Greer, B. M., Burbey, T. J., Zipper, C. E., and Hester, E. T.: Electrical resistivity imaging of hydrologic flow through surface coal mine valley fills with comparison to other landforms, Hydrol. Process., 31, 2244–2260, https://doi.org/10.1002/hyp.11180, 2017.

Gu, W.-Z., Liu, J.-F., Lin, H., Lin, J., Liu, H.-W., Liao, A.-M., Wang, N., Wang, W.-Z., Ma, T., Yang, N., Li, X.-G., Zhuo, P., and Cai, Z.: Why Hydrological Maze: The Hydropedological Trigger? Review

https://doi.org/10.5194/hess-2023-190
Preprint. Discussion started: 29 August 2023

of Experiments at Chuzhou Hydrology Laboratory, Vadose Zone J, 17, 1–27, https://doi.org/10.2136/vzj2017.09.0174, 2018.

Guo, L., Mount, G. J., Hudson, S., Lin, H., and Levia, D.: Pairing geophysical techniques improves understanding of the near-surface Critical Zone: Visualization of preferential routing of stemflow along coarse roots, Geoderma, 357, 113953, https://doi.org/10.1016/j.geoderma.2019.113953, 2020.

Hermans, T., Goderniaux, P., Jougnot, D., Fleckenstein, J. H., Brunner, P., Nguyen, F., Linde, N., Huisman, J. A., Bour, O., Lopez Alvis, J., Hoffmann, R., Palacios, A., Cooke, A.-K., Pardo-Álvarez, Á., Blazevic, L., Pouladi, B., Haruzi, P., Fernandez Visentini, A., Nogueira, G. E. H., Tirado-Conde, J., Looms, M. C., Kenshilikova, M., Davy, P., and Le Borgne, T.: Advancing measurements and representations of subsurface heterogeneity and dynamic processes: towards 4D hydrogeology, Hydrol. Earth Syst. Sci., 27, 255–287, https://doi.org/10.5194/hess-27-255-2023, 2023.

Hojat, A., Arosio, D., Ivanov, V. I., Longoni, L., Papini, M., Scaioni, M., Tresoldi, G., and Zanzi, L.: Geoelectrical characterization and monitoring of slopes on a rainfall-triggered landslide simulator, J Appl Geophy, 170, 103844, https://doi.org/10.1016/j.jappgeo.2019.103844, 2019.

Holbrook, W. S., Riebe, C. S., Elwaseif, M., L. Hayes, J., Basler-Reeder, K., L. Harry, D., Malazian, A., Dosseto, A., C. Hartsough, P., and W. Hopmans, J.: Geophysical constraints on deep weathering and water storage potential in the Southern Sierra Critical Zone Observatory, Earth Surf. Process. Landforms, 39, 366–380, https://doi.org/10.1002/esp.3502, 2014.

Linde, N., Doetsch, J., Jougnot, D., Genoni, O., Dürst, Y., Minsley, B. J., Vogt, T., Pasquale, N., and Luster, J.: Self-potential investigations of a gravel bar in a restored river corridor, Hydrol. Earth Syst. Sci., 15, 729–742, https://doi.org/10.5194/hess-15-729-2011, 2011.

Luongo, R., Perrone, A., Piscitelli, S., and Lapenna, V.: A Prototype System for Time-Lapse Electrical Resistivity Tomographies, International Journal of Geophysics, 2012, 1–12, https://doi.org/10.1155/2012/176895, 2012.

Nielson, T., Bradford, J., Pierce, J., and Seyfried, M.: Soil structure and soil moisture dynamics inferred from time-lapse electrical resistivity tomography, Catena, 207, 105553, https://doi.org/10.1016/j.catena.2021.105553, 2021.

https://doi.org/10.5194/hess-2023-190
Preprint. Discussion started: 29 August 2023

Hydrology and Earth System Sciences
Discussions

Nimmer, R. E., Osiensky, J. L., Binley, A. M., Sprenke, K. F., and Williams, B. C.: Electrical resistivity imaging of conductive plume dilution in fractured rock, Hydrogeol J, 15, 877–890, https://doi.org/10.1007/s10040-007-0159-z, 2007.

Oldenburg, D. W. and Li, Y.: Estimating depth of investigation in dc resistivity and IP surveys, Geophysics, 64, 403–416, https://doi.org/10.1190/1.1444545, 1999.

Parsekian, A. D., Singha, K., Minsley, B. J., Holbrook, W. S., and Slater, L.: Multiscale geophysical imaging of the critical zone: Geophysical Imaging of the Critical Zone, Rev. Geophys., 53, 1–26, https://doi.org/10.1002/2014RG000465, 2015.

Revil, A., Karaoulis, M., Johnson, T., and Kemna, A.: Review: Some low-frequency electrical methods for subsurface characterization and monitoring in hydrogeology, Hydrogeol J, 20, 617–658, https://doi.org/10.1007/s10040-011-0819-x, 2012.

Richards, K., Revil, A., Jardani, A., Henderson, F., Batzle, M., and Haas, A.: Pattern of shallow ground water flow at Mount Princeton Hot Springs, Colorado, using geoelectrical methods, J. Volcanol. Geotherm. Res., 198, 217–232, https://doi.org/10.1016/j.jvolgeores.2010.09.001, 2010.

Robinson, J. L., Slater, L. D., and Schäfer, K. V. R.: Evidence for spatial variability in hydraulic redistribution within an oak–pine forest from resistivity imaging, J. Hydrol., 430–431, 69–79, https://doi.org/10.1016/j.jhydrol.2012.02.002, 2012.

Sidle, R. C., Noguchi, S., Tsuboyama, Y., and Laursen, K.: A conceptual model of preferential flow systems in forested hillslopes: evidence of self-organization, Hydrol. Process., 15, 1675–1692, https://doi.org/10.1002/hyp.233, 2001.

Srayeddin, I. and Doussan, C.: Estimation of the spatial variability of root water uptake of maize and sorghum at the field scale by electrical resistivity tomography, Plant Soil, 319, 185–207, https://doi.org/10.1007/s11104-008-9860-5, 2009.

Suski, B., Revil, A., Titov, K., Konosavsky, P., Voltz, M., Dagès, C., and Huttel, O.: Monitoring of an infiltration experiment using the self-potential method, Water Resour. Res., 42, https://doi.org/10.1029/2005WR004840, 2006.

https://doi.org/10.5194/hess-2023-190
Preprint. Discussion started: 29 August 2023

Hydrology and Earth System Sciences
Discussions

Tetzlaff, D., Birkel, C., Dick, J., Geris, J., and Soulsby, C.: Storage dynamics in hydropedological units control hillslope connectivity, runoff generation, and the evolution of catchment transit time distributions, Water Resour. Res., 50, 969–985, https://doi.org/10.1002/2013WR014147, 2014.

Travelletti, J., Sailhac, P., Malet, J.-P., Grandjean, G., and Ponton, J.: Hydrological response of weathered clay-shale slopes: water infiltration monitoring with time-lapse electrical resistivity tomography, Hydrol. Process., 26, 2106–2119, https://doi.org/10.1002/hyp.7983, 2012.

Tsai, W.-N., Chen, C.-C., Chiang, C.-W., Chen, P.-Y., Kuo, C.-Y., Wang, K.-L., Lin, M.-L., and Chen, R.-F.: Electrical Resistivity Tomography (ERT) Monitoring for Landslides: Case Study in the Lantai Area, Yilan Taiping Mountain, Northeast Taiwan, Front. Earth Sci., 9, 737271, https://doi.org/10.3389/feart.2021.737271, 2021.

Vanella, D., Cassiani, G., Busato, L., Boaga, J., Barbagallo, S., Binley, A., and Consoli, S.: Use of small scale electrical resistivity tomography to identify soil-root interactions during deficit irrigation, J. Hydrol., 556, 310–324, https://doi.org/10.1016/j.jhydrol.2017.11.025, 2018.

Voytek, E. B., Rushlow, C. R., Godsey, S. E., and Singha, K.: Identifying hydrologic flowpaths on arctic hillslopes using electrical resistivity and self potential, Geophysics, 81, WA225–WA232, https://doi.org/10.1190/geo2015-0172.1, 2016.

Voytek, E. B., Barnard, H. R., Jougnot, D., and Singha, K.: Transpiration- and precipitation-induced subsurface water flow observed using the self-potential method, Hydrol. Process., hyp.13453, https://doi.org/10.1002/hyp.13453, 2019.

Wang, H., Fu, S.J., Ge, S.Y., Ma, F.Y., Song, B.Y., and Luo, J.C..: Development and performance testing of maintenance free ultra-low noise solid unpolarized electrodes. Geophysical and Geochemical Exploration, 46 (3): 714-721, https://doi.org/10.11720/wtyht. 2022.1386, 2022.

Zeng, R. Q., Meng, X. M., Zhang, F. Y., Wang, S. Y., Cui, Z. J., Zhang, M. S., Zhang, Y., and Chen, G.: Characterizing hydrological processes on loess slopes using electrical resistivity tomography – A case study of the Heifangtai Terrace, Northwest China, J. Hydrol., 541, 742–753, https://doi.org/10.1016/j.jhydrol.2016.07.033, 2016.

https://doi.org/10.5194/hess-2023-190
Preprint. Discussion started: 29 August 2023

673 Zhou, Q. Y., Shimada, J., and Sato, A.: Three-dimensional spatial and temporal monitoring of soil water
674 content using electrical resistivity tomography, Water Resour. Res., 37, 273–285,
675 https://doi.org/10.1029/2000WR900284, 2001.
676